INSTITUTE OF PHYSICS PUBLISHING JOURNAL OF PHYSICS: CONDENSED MATTER

J. Phys.: Condens. Matter **16** (2004) S1041–S1052 PII: S0953-8984(04)74910-3

Single-crystal elasticity of andradite garnet to 11 GPa

Fuming Jiang, Sergio Speziale, Sean R Shieh and Thomas S Duffy

Department of Geosciences, Princeton University, Princeton, NJ 08544, USA

Received 21 January 2004
Published 26 March 2004
Online at stacks.iop.org/JPhysCM/16/S1041
DOI: 10.1088/0953-8984/16/14/014

Abstract

The high-pressure elastic properties of single-crystal andradite garnet $Ca_3Fe_2^{3+}Si_3O_{12}$ were determined by Brillouin scattering to 11 GPa. The pressure dependence of the elastic stiffness constants and aggregate bulk and shear moduli were obtained by inversion of the data to finite Eulerian strain equations. The inversion yields $C_{11} = 286.7 \pm 0.6$ GPa, $C_{12} = 88.6 \pm 0.6$ GPa, $C_{44} = 83.8 \pm 0.3$ GPa, $K_{0S} = 154.5 \pm 0.6$ GPa, $G_{0S} = 89.7 \pm 0.4$ GPa, $(\partial K_{0T}/\partial P)_T = 4.71 \pm 0.1$, and $(\partial G_0/\partial P)_T = 1.25 \pm 0.05$. Both individual and aggregate elastic moduli define nearly linear modulus–pressure trends. The elastic anisotropy of andradite garnets increases weakly in magnitude with compression. Previous studies of the high-pressure elasticity of andradite garnet are highly discrepant, with reported pressure derivatives of the bulk modulus varying by 46% and pressure derivatives of the shear modulus varying by 253%. We are able to provide plausible explanations for these discrepancies. In particular, differences between previous x-ray diffraction data and a static compression curve constructed from our Brillouin data can be attributed to the effects of non-hydrostatic stresses on the x-ray data.

1. Introduction

Over the last two decades, great effort has been dedicated to characterizing the elastic properties of materials at high pressures, especially minerals relevant to the Earth's mantle [1]. With the recent development of new x-ray, ultrasonic, and spectroscopic techniques for elastic tensor determination, the interest in elastic properties at high pressures has further intensified [2–4]. The results of such studies have direct applications to understanding the structure, composition, and mineralogy of the Earth's interior [5].

A large number of compounds crystallize in the garnet ($X_3Y_2Z_3O_{12}$) structure. Silicate garnets are important constituents of metamorphic rocks as well as the Earth's upper mantle and transition zone. The elastic properties of garnets are of interest not only because of their geological relevance but also due to their myriad technological applications [6]. Because of the existence of large, well formed natural single crystals, together with their high symmetry and wide compositional range, the elastic properties of garnets have been

 © 2004 IOP Publishing Ltd Printed in the UK

Table 1. Andradite microprobe analysis. (Note: end-member mol%, andradite—0.98; grossular—0.017; pyrope—0.003; other—trace. Lattice parameter was determined by powder x-ray diffraction. All Fe reported as FeO.)

	SiO_2	FeO	CaO	MgO	MnO	Al_2O_3	Lattice parameter
wt%	35.988	28.211	33.6165	0.056	0.056	0.419	12.0565 Å

studied far more extensively than any other silicate mineral group (see [7] for a compilation of earlier studies). Andradite garnet ($Ca_3Fe_2Si_3O_{12}$) is of interest because it forms a solid solution with grossular ($Ca_3Al_2Si_3O_{12}$) garnet, and thus allows for investigation of the effect of $Al^{3+} \leftrightarrows Fe^{3+}$ substitution on the elastic properties of silicates.

The silicate garnet group $X_3Y_2(SiO_4)_3$ includes a series of isostructural species with space group $Ia3d$, where the X site houses Ca^{2+}, Mg^{2+}, Fe^{2+}, or Mn^{2+} and the Y site incorporates Al^{3+}, Fe^{3+}, and Cr^{3+}; they crystallize in the hexoctahedral class of the isometric system and are similar in crystal habit. The unit cell of garnet contains eight formula units. The structure consists of alternating ZO_4 tetrahedra and YO_6 octahedra which share corners to form a three-dimensional network [8]. Andradite-rich compositions containing more than 90 mol% of andradite are fairly common. Grossular very close to the end-member composition can occur, and its predominant substitutional component is andradite, with which it forms a continuous series.

The elastic properties of andradite garnets have been the subject of extensive study in recent years. While reported values for the ambient-pressure elastic properties are consistent, the results of different experiments at high pressure are in poor agreement. Such discrepancies greatly hinder efforts to systematically describe the high-pressure elastic properties of garnets as a function of composition. In this study, we report detailed Brillouin scattering measurements on a natural crystal of andradite to 11 GPa. Our results disagree with previous high-pressure studies of andradite garnet. Our study has advantages over the previous work, and thus we are able to greatly clarify the high-pressure elastic properties of this important end-member garnet.

2. Experimental details

Natural andradite single-crystal samples were obtained from Yellow Cat Mine, San Benito County, California. They showed characteristic dodecahedral habits. Platelets parallel to the natural (110) faces were cut with a diamond saw and then double-side polished with successively finer grits down to a final diamond paper of 1 μm particle size. We developed a polishing scheme that ensures tilting of the top and bottom surfaces of the sample with an order of 10^{-3} degrees. The final sample thickness was approximately 30 μm. The polished crystal samples were checked under a polarizing microscope, and there was no sign of zoning. The composition of the sample used for our Brillouin experiment was determined by microprobe analysis. Ten points were analysed across the sample, and they have almost the same composition. Table 1 shows the average composition from the analysed points. The sample was loaded into a modified Merrill–Bassett diamond anvil cell (DAC) [9] with a 96° aperture. The sample was compressed between two 500 μm diamond culets, and a 16:3:1 volume mixture of methanol–ethanol–water (M–E–W) was used as a pressure transmitting medium. Several ruby chips were placed around the sample for pressure determination. Pressure differences at different positions never exceeded ± 0.2 GPa.

Brillouin scattering experiments were performed in a symmetric forward scattering geometry, in which acoustic mode velocities can be determined without knowledge of the sample refractive index [10]. The sample was excited using a vertically polarized neodymium

doped yttrium vanadate laser (λ= 532.15 nm) with a power of 150 mW, and spectra were measured using a six-pass Sandercock tandem Fabry–Perot interferometer, and recorded by a solid-state photon detector with 70% quantum efficiency [11]. Special attention was paid to determining the scattering angle to within a few minutes of a degree using a reference laser beam. The accuracy, precision, and reproducibility of our system were tested on standard single crystals of MgO and $SrTiO_3$ with known velocities [12]. The same procedure as used in this study was applied to a (100)-cut MgO single crystal from MTI corporation; the phonon-propagation plane calculated using fitted Eulerian angles (θ_0, φ_0, χ_0) was exactly (100), and the elastic constants obtained are $C_{11} = 297.1 \pm 0.2$ GPa, $C_{12} = 95.4 \pm 0.2$ GPa, and $C_{44} = 155.4 \pm 0.1$ GPa. They are in close agreement with literature values with an uncertainty less than 0.5% [12–14]. A significant error in velocity determination can be caused by vignetting due to the limited aperture of the DAC [12]. In this case, some portion of the scattered or incident light cone can be blocked by DAC supports or gasket, resulting in asymmetric Brillouin lineshapes and systematically low frequency shifts. A diaphragm was added in front of the collection lens to prevent vignetting. It was closed successively until symmetric lineshapes were obtained and Brillouin peak positions remained the same upon further closing of the aperture. On the incident side, there was no vignetting effect because of smaller incident beam diameter.

In Brillouin experiments, the scattered intensity is proportional to [15]

$$I(\omega) \propto [E_s^T \cdot (T_{ij}) \cdot E_i]^2, \tag{1}$$

where E_i and E_s are polarization directions of incident and scattered light and T_{ij} is the elasto-optic tensor component. The above equation determines the Brillouin selection rules, e.g., what acoustic modes can appear in a certain scattering geometry. To improve the quality of our Brillouin spectrum, a $\lambda/2$ plate was inserted into the incident light path, and the Brillouin spectrum was 'tuned' to optimum intensity by rotating the $\lambda/2$ plate, causing a variation of incident polarization E_i. An example is shown in figure 1 for our andradite sample. Based on the selection rules, some 'invisible' acoustic modes could be uncovered by varying E_i, and our experimental accuracy in determining acoustic velocities was improved.

3. Results and discussion

Andradite crystallizes in the cubic system (space group $Ia3d$) and hence has three independent non-zero elastic constants: C_{11}, C_{12}, and C_{44}. Brillouin scattering measurements in one or two special directions are the minimum needed if all three acoustic modes can be observed in a given crystallographic direction. In practice, usually one quasi-longitudinal acoustic mode and a quasi-transverse acoustic mode are observed in symmetry planes. In addition, for the forward scattering geometry, it is difficult to assign the quasi-transverse acoustic mode to the fast or slow branch without knowing the components of the elasto-optic tensor. Incorrect assignment of the transverse acoustic mode to a specific branch would result in incorrect elastic constants. Therefore, in our experiments, Brillouin spectra were collected over 36 crystallographic directions in a single plane at each of nine pressures from room pressure to 11 GPa. As discussed below, the procedure used to derive the constants is self-consistent and densities are obtained from Brillouin measurements as well. Figure 2 shows a typical Brillouin spectrum at 8.69 GPa. In all measured directions, only one quasi-longitudinal and one quasi-transverse acoustic mode were observed.

Acoustic velocities, V, in the forward scattering geometry are determined by [10]

$$V = \frac{\Delta\nu\lambda_0}{2\sin\alpha}, \tag{2}$$

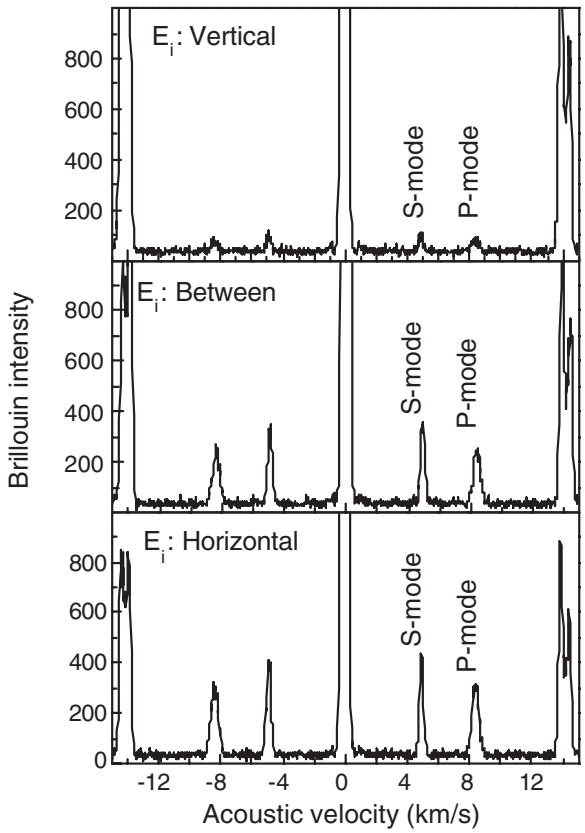

Figure 1. Polarized Brillouin spectra at room pressure. The polarization of the incident light E_i was adjusted by inserting a half waveplate into the incident light path.

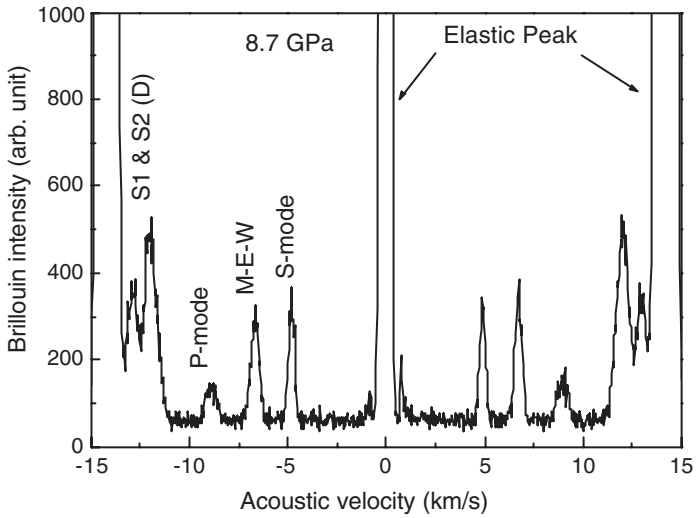

Figure 2. Brillouin spectrum of andradite at 8.7 GPa: the P-mode and S-mode are quasi-longitudinal and quasi-transverse modes of andradite; M–E–W peaks are from the pressure medium; and S1 and S2 are two shear modes of diamond (D).

Table 2. Best-fit density, elastic constants, and aggregate moduli of andradite. Numbers in parenthesis are 1σ standard deviations in the last digits; RMS, root mean square of the difference between observed and calculated sound velocities. (Note: Average $(\theta_0, \varphi_0, \chi_0) \sim (44.4° \pm 1, 31.5° \pm 2, 90.7° \pm 2)$; $(hkl) \sim (0.01, 0.98, 1.00)$.)

P (GPa)	ρ (g cm^{-3})	C_{11} (GPa)	C_{12} (GPa)	C_{44} (GPa)	K_S (GPa)	G_S (GPa)	RMS (m s^{-1})
0.0001	3.843	284.0(6)	88.1(6)	82.9(3)	154.5(6)	88.6(4)	24
1.0	3.867	294.7(6)	93.2(4)	85.6(2)	160.3(5)	91.4(3)	21
2.5	3.903	304.3(4)	95.7(3)	86.7(2)	165.2(3)	93.3(3)	14
3.3	3.921	311.6(6)	99.7(5)	86.4(3)	170.3(5)	93.8(4)	22
5.7	3.977	324.9(7)	109.5(5)	89.1(3)	181.3(6)	96.2(4)	22
7.3	4.012	338.3(6)	114.1(5)	91.0(3)	188.8(5)	98.9(4)	22
8.7	4.041	345.5(7)	117.6(5)	91.5(3)	193.6(6)	99.9(4)	22
10.4	4.076	355.1(7)	123.0(5)	92.5(3)	200.4(6)	101.3(4)	21
11.2	4.092	362.1(8)	126.8(5)	93.6(3)	205.3(6)	102.6(4)	21

where λ_0 is the incident laser wavelength, $\Delta\nu$ is the measured Brillouin frequency shift, and α is the incidence angle external to the diamond anvil cell. In all measurements, a 35° external incidence angle was used. The horizontal axis in figures 1 and 2 was converted into velocity from the measured frequency shift using the above equation.

To extract the elastic constants from the measured acoustic velocities at each pressure, analytical expressions derived from Christoffel's equation for the three acoustic modes were used [16]. ρV_j^2 is expressed as a function of six parameters:

$$\rho V_j^2 = f_j(C_{11}, C_{12}, C_{44}, q_x, q_y, q_z), \tag{3}$$

where ρ is density, the subscript j (=0, 1, 2) indicates the longitudinal acoustic mode (V_{P}), slow transverse acoustic mode (V_{S1}), and fast transverse acoustic mode (V_{S2}), respectively, and q_x, q_y, and q_z are direction cosines of the phonon wavevector in the crystal coordinate system. Our experimental system is similar to that described in the literature [17], and the three Euler angles $(\theta_0, \varphi_0, \chi_0)$ relating the crystallographic coordinate system to the laboratory coordinate system were used to describe the phonon wavevector direction (q_x, q_y, q_z). The azimuthal angle φ was the only one varied during measurement, and hence the φ-value for a given phonon direction is described by $\varphi_0 + \varphi_i$, where φ_i represents the change in φ for a given measurement, i, from its starting value φ_0. A least-squares fit between calculated $f_j(\varphi_i)$ and experimental velocities V_{ji} as a function of angle φ_i was computed:

$$\chi^2 = \sum_{ij} [f_j(C_{11}, C_{12}, C_{44}, \theta_0, \varphi_0 + \varphi_i, \chi_0) - V_{ji}(\varphi_i)]^2. \tag{4}$$

χ^2 was minimized in two steps. First, we systematically varied all six parameters with a grid search to find the best starting model. The results of the grid search were then used in a non-linear least-squares inversion to obtain the final model. Since only one shear mode was observed in our Brillouin spectra, a trial-and-error approach was used to assign the measured shear mode velocities to V_{S1} and V_{S2}, respectively, until satisfactory agreement between calculated $f_j(\varphi_i)$ and experimentally obtained velocities $V_{ji}(\varphi_i)$ was attained. The subscript i indicates the velocity at angle φ_i. An additional check was made by calculating the plane of the crystal platelet using the average fitted Euler angles $(\theta_0, \varphi_0, \chi_0)$, which is $(hkl) \sim (0.01, 0.98, 1.00)$. The deviations of Euler angles at all pressures never exceed ±2° (see table 2). The crystal used in our experiment was cut from a natural (110) surface, thus it confirms that our fitting procedures are self-consistent and reliable. The dependence of acoustic velocity on direction in the measured plane at room pressure and 8.69 GPa is shown in figure 3.

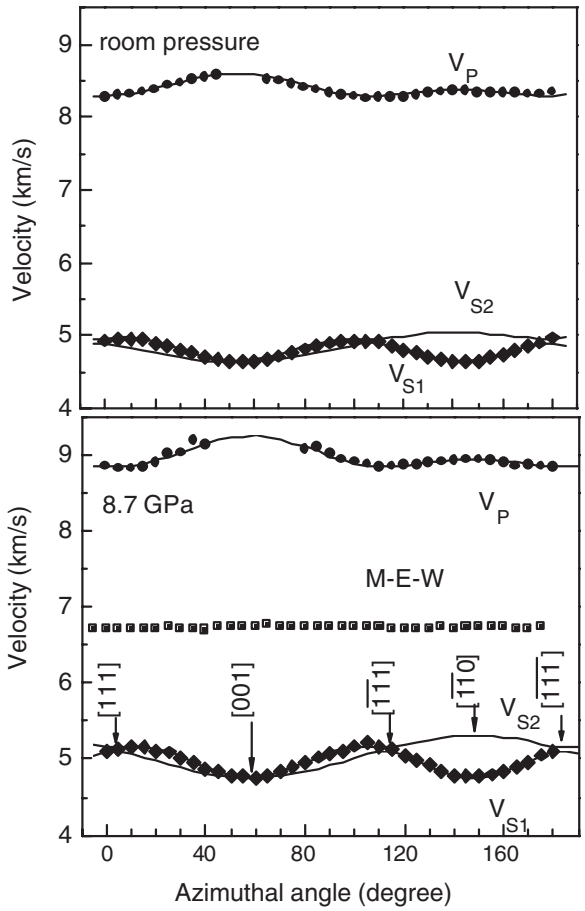

Figure 3. Velocities in a plane close to (110) at room pressure and 8.7 GPa as a function of crystallographic direction. The azimuthal angle is relative to an arbitrary starting direction. The solid curves are calculated using best-fit elastic constants. Velocities from the M–E–W pressure medium are also plotted. The locations of directions [100], [110], and [111] are marked.

It is clear that the experimentally obtained acoustic velocities closely lie on the theoretically calculated velocity curves. The root-mean-square (RMS) deviations between measured and calculated velocities vary between 14 and 24 m s^{-1}, indicating excellent agreement between measured and calculated velocities. If all the observed shear modes were attributed to each one of the two V_S modes, no satisfactory fit could be obtained between experimental and calculated velocities. This is clearly reflected in the RMS between the observed and calculated velocities. At room pressure, if all the shear modes are attributed to the slow and fast shear branches, the RMSs of the fitting are 39 and 51 m s^{-1}, respectively. These are 63% and 113% larger in comparison with the 24 m s^{-1} obtained from our fitting approach. This justifies our treatment of the mode assignment. The RMS deviations of the fitting of our measured velocities in table 2 are similar to or better than those reported in the literature [18–21]. The experimentally measured velocities of the M–E–W pressure medium were also plotted in figure 3, and they follow a straight line as expected since the fluid pressure medium is isotropic.

In the inversion of high-pressure moduli, an iterative procedure [11, 18] was adopted to determine the third-order Eulerian finite strain parameters [22–24] for the individual and

Table 3. Thermodynamic and thermoelastic parameters of andradite at ambient conditions.

Parameters	Value	References
Thermal expansion, α_0 (K^{-1})	20.6×10^{-6}	[25]
Grüneisen parameter, γ_0	1.2	Calculated[a]
Specific heat, C_P (J mol^{-1} K^{-1})	351.9(7)	[26]
$(\partial K_{0T}/\partial T)_p$ (GPa K^{-1})	−0.0243	[27][b]

[a] Grüneisen parameter obtained as $\gamma_0 = \alpha_0 K_{0S}/(\rho_0 C_P)$ using K_{0S} and ρ_0 of this study.
[b] $(\partial K_{0T}/\partial T)_p$ was extrapolated from that of grossular–andradite samples.

Table 4. Elastic constants at room pressure, and their pressure derivatives from the third-order Eulerian finite-strain fits. Numbers in parenthesis are 1σ deviations in the last digits.

Study	C_{11} (GPa)	C_{12} (GPa)	C_{44} (GPa)	$\partial C_{11}/\partial P$	$\partial C_{12}/\partial P$	$\partial C_{44}/\partial P$
This study	286.7(6)	88.6(6)	83.8(3)	7.06(14)	3.47(8)	0.99(5)
[19]	289(2)	92(2)	85(1)			
[30] [a]	268.7(26)	72.7(22)	82.7(10)			

[a] Extrapolated from a sample of composition $And_{70.4}Grs_{22.2}Alm_{4.1}Pyr_{2.8}Sps_{0.5}Uvr_{0.1}$.

Table 5. Adiabatic, isothermal moduli at room pressure and their pressure deratives. Numbers in parenthesis are 1σ deviations in the last digits. (Note: BS—Brillouin scattering; X—x-ray diffraction; U—polycrystalline ultrasonic elasticity.)

References	K_{0S} (GPa)	K_{0T} (GPa)	$\partial K_{0S}/\partial P$	$\partial K_{0T}/\partial P$	G_0 (GPa)	$\partial G_0/\partial P$	Method
This study	154.5(6)	153.4(6)	4.70(10)	4.71(10)	89.7(4)	1.25(5)	BS
[32]	159.4	158.3	5.85			4.3	BS
[19]	157(2)				90(1)		BS
[30]	137.9(17)				88.5(16)		U
[35]		159(2)		4[a]			X
[34]		157(1)		5.1[a]			X
[33]		158.5(10)		5.77(10)			X
[7]	162.5(23)		4.7(3)		86.0(3)	1.7(3)	U

[a] Fixed values.

aggregate elastic moduli as well as the density at each pressure. The adiabatic aggregate bulk modulus is given by $K_S = (C_{11} + 2C_{12})/3$ and the aggregate shear modulus was obtained using the Voigt–Reuss–Hill (VRH) averaging method (table 2). An initial density model was used to obtain the ambient-pressure values of the adiabatic bulk modulus, K_{0S}, and its first pressure derivative, $(\partial K_{0S}/\partial P)_T$, from a least-squares fit to the finite-strain equation [23, 24]. These values were then converted to isothermal values of K_{0T} and $(\partial K_{0T}/\partial P)_T$ using known values from thermodynamic parameters [25–27]. The isothermal bulk modulus was calculated by applying the thermodynamic relation $K_{0T} = K_{0S}/(1 + \alpha\gamma T)$, where α is the volume thermal expansion coefficient and γ is the Grüneisen parameter [25, 26] (table 3). The pressure derivative of the isothermal bulk modulus at standard conditions was calculated using the relation $(\partial K_{0T}/\partial P)_T \approx (1 + \alpha\gamma T)^{-1}[(\partial K_{0S}/\partial P)_T - \gamma T/K_T(\partial K_{0T}/\partial T)_P]$. The isothermal parameters were then used to construct isothermal compression curves using the Birch–Murnaghan equation and obtain refined densities. The procedure was repeated and it converged after four iterations. Fit results for densities, elastic constants and calculated aggregate moduli at each pressure are listed in table 2.

The final individual and aggregate moduli were fitted to Eulerian finite strain equations to determine their pressure derivatives (tables 4 and 5). Figures 4 and 5 show the pressure

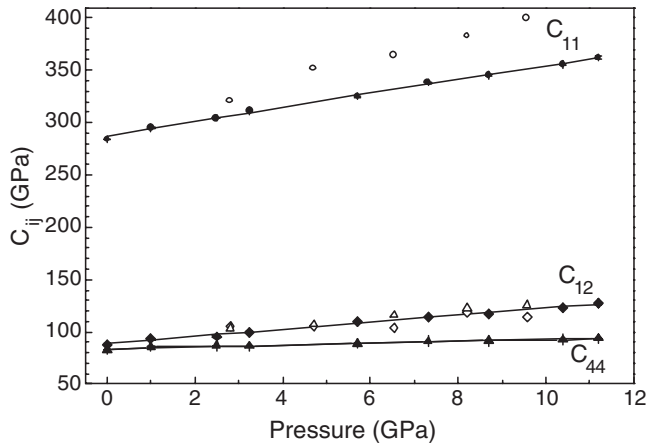

Figure 4. Elastic stiffness constants C_{11}, C_{12}, and C_{44} versus pressure: filled symbols, this study; open symbols, [32]; solid lines are fits to our results using finite-strain theory.

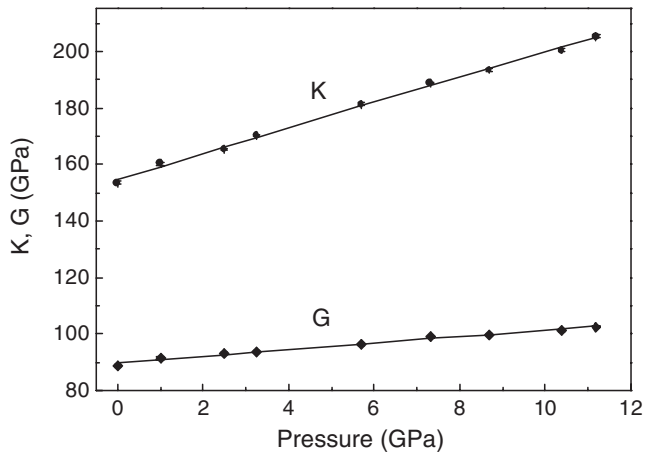

Figure 5. Elastic moduli of andradite K_S and G_S versus pressure: solid lines are fits to our results using finite-strain theory.

dependences of our elastic stiffness constants and the calculated aggregate moduli. The solid lines are fits to our results using finite-strain theory. The individual moduli define nearly linear trends with pressure consistent with earlier studies of garnets in the pyrope–almandine–grossular system [12, 28], although in comparison with these garnets, andradite has larger values of $\partial C_{11}/\partial P$ and $\partial C_{12}/\partial P$, but a smaller value of $\partial C_{44}/\partial P$. The former results in a higher value of $\partial K_{0S}/\partial P$ for andradite compared to these other garnets. Since andradite has a lower bulk modulus at ambient conditions, the effect of pressure is then to reduce the difference in K_S between andradite and the other garnets. The elastic anisotropy, $2C_{44}/(C_{11} - C_{12})$, increases in magnitude weakly with pressure from 0.85 at room pressure to 0.80 at 11 GPa.

The fit value of our adiabatic bulk modulus at ambient condition is 154.5 GPa, which is 2 GPa lower than the 157 GPa reported for another andradite $An_{96}Gr_{3.7}Py_{0.3}$ with 3.7% grossular also using Brillouin scattering [19], while our andradite is $An_{98}Gr_{1.7}Py_{0.3}$. Andradite

has the slowest acoustic velocity among all garnet end members [19]. The bulk modulus K_{0S} of grossular determined by Brillouin scattering was 168.4 GPa [29]. The small compositional differences between our sample and that of Bass [19] would be expected to produce a difference in modulus much less than experimental error. All the individual C_{ij} as well as the bulk and shear moduli overlap Bass's [19] values at the 1σ level except for C_{12}, for which Bass's value is 3.8% higher than ours. The K_{0S}-value from Babuška *et al* [30] of 138±2 GPa, in which the K_{0S}-value was extrapolated from solid solution values, is much lower than found in other studies. As discussed in [19], this suggests possible non-linearities in the bulk modulus–composition relation for the grossular–andradite series. Further measurements are necessary to confirm this. The bulk modulus from Wang and Ji [7], $K_{0S} = 162.5$ GPa, for a polycrystalline sample measured using the ultrasonic method is 5% larger than ours, and their pressure derivative ($K'_{0S} = 4.7$) is consistent with our value. A theoretical study [31] of andradite using density functional theory reported a bulk modulus of 147 GPa and a pressure derivative of 4.4; both of these are in agreement with our results within the ∼10% accuracy of theoretical calculations.

The high-pressure elastic stiffness constants and bulk and shear moduli obtained in this study are lower than those reported by Conrad *et al* [32] who also used Brillouin scattering, and it is not easy to explain the discrepancy (figure 4, table 5). The compressional and shear acoustic velocities from Conrad *et al* along [100] and [110] are much higher than ours and the discrepancy increases with pressure. For example, at 9.6 GPa, the compressional and shear sound velocities Conrad *et al* along [100] are 6% and 19% higher than our results, respectively. Consequently, all their inverted elastic stiffness constants are higher except for C_{12} (figure 4). Such large discrepancies suggest possible systematic errors in spectrometer calibration, scattering angle, or pressure calibration. It is also possible that sample bridging resulted in increasing degrees of non-hydrostatic stress with compression. In their Brillouin experiments, two special acoustic wavevector directions [110] and [100] were used to determine the acoustic velocities and elastic constants. Andradite has one pure V_P ($\rho V_P^2 = C_{11}$) and two degenerate V_S modes ($\rho V_{S1}^2 = \rho V_{S2}^2 = C_{44}$) when acoustic waves are propagating along [100] crystallographic directions, and has one pure LA ($\rho V_P^2 = (C_{11} + C_{12} + 2C_{44})/2$) and two non-degenerate V_S modes ($\rho V_{S1}^2 = C_{44}$, $\rho V_{S2}^2 = (C_{11} - C_{12})/2$) along [110] directions (see figure 3). Conrad *et al* [32] assigned the observed shear mode to $\rho V_{S2}^2 = (C_{11} - C_{12})/2$ instead of $\rho V_{S2}^2 = C_{44}$ for the wavevector direction [110], and except at the lowest pressure their acoustic velocities at different pressures are nearly the same for [100] and [110] directions. This again contrasts sharply with our observations in which the P-velocities along [100] and [110] differ by about 3–4% and the S-velocities along [100] ($\sqrt{C_{44}/\rho}$) and [110] ($\sqrt{(C_{11} - C_{12})/2\rho}$) differ by 8–12%. This suggests possible orientation or mode assignment errors, as the other shear branch along [110] is the same as the degenerate modes along [100]. Our results in both absolute velocity and in velocity differences between [100] and [110] are consistent with ambient-pressure data [19]. The large number of measured directions, and successful inversion for the expected crystal orientation, also support the present measurements.

Figure 6 shows a comparison of the volume compression curve calculated using the present Brillouin data with earlier static compression studies. At pressures below 4 GPa, our results are in good agreement with earlier studies, but the powder x-ray diffraction results of Pavese *et al* [33] and Zhang *et al* [34] become increasingly less compressible than our P–V curve and its extrapolation at higher pressures. The single-crystal results of Hazen and Finger [35], while exhibiting a higher degree of scatter than other studies, are in better agreement with our results. Determination of elastic properties from static compression studies suffers from several limitations in comparison with Brillouin scattering. The determination of the bulk modulus and its pressure derivative from static compression relies on fits to the slope of the measured P–V curve, and hence are less direct than Brillouin measurements. Static compression studies also

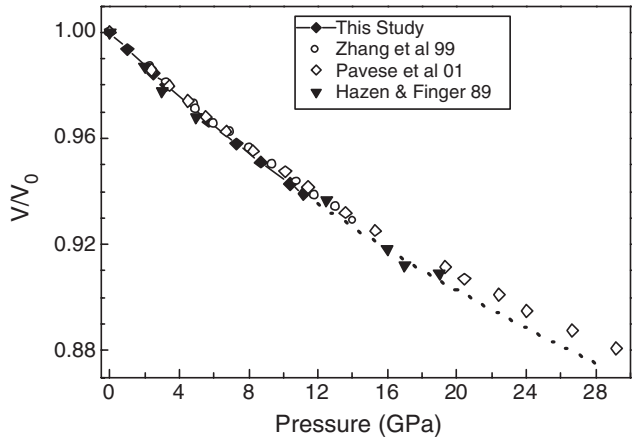

Figure 6. Pressure–volume curve derived from our Brillouin measurement together with static compression data from a variety of sources. The solid curve (dashed where extrapolated) is derived from the present Brillouin data.

suffer from a well known trade-off between fit values for K_{0T} and K'_{0T}. Thus, a larger pressure range is required for reliable constraints on K_{0T} and K'_{0T} when using static compression. However, higher pressure usually leads to the presence of deviatoric stresses in the sample chamber which is known to produce systematic underestimation of compressibility in the diamond anvil cell. The pressure media used in the previous studies (N_2—[33], Ne—[35, 34]) result in non-hydrostatic stresses above 3 and 4.5 GPa, respectively, due to freezing of the pressure medium. In contrast, the methanol–ethanol–water medium used in this study remains strictly hydrostatic over the entire measured pressure range. The static compression studies obtain values of K_{0T} in agreement with earlier ambient-pressure Brillouin results [19], but the pressure derivatives of the bulk modulus (which was either fixed or a fitting parameter) vary by $\sim$44%. This large range is a consequence of the effects of both deviatoric stresses and the limited P–V coverage of the data.

Wang and Ji [7] reported the results of an ultrasonic study of the aggregate elastic properties of polycrystalline andradite to 3 GPa using a piston–cylinder device. While the pressure derivatives of the bulk moduli overlap within uncertainty, the bulk modulus obtained here is 5% lower than found by Wang and Ji [7]. Our results are in good agreement with the work of Bass [19] as discussed earlier. In general, ultrasonic studies using polycrystalline samples are subject to uncertainties due to sample quality, especially when the pressure range is very limited.

The andradite ($Ca_3Fe_2Si_3O_{12}$)–grossular ($Ca_3Al_2Si_3O_{12}$) solid solution is characterized by a simple substitution of Fe^{3+} for Al^{3+} on the octahedral site. The larger ionic radius of Fe^{3+} in comparison with Al^{3+} results in expansion of the structure as reflected in the lattice parameter (andradite, 12.058 Å; grossular, 11.845 Å) [8] and a reduction in the bulk modulus (andradite, 155 GPa; grossular, 168 GPa [29]). Measurements of the high-pressure elastic properties of grossular are in progress that will allow us to assess how pressure affects the variation in elastic properties across this solid solution.

4. Conclusions

Brillouin scattering to 11 GPa was carried out to determine the high-pressure elastic properties of an andradite-rich (An_{98}) garnet. Individual and aggregate elastic moduli display nearly linear

trends with pressure. The aggregate adiabatic bulk and the Voigt–Reuss–Hill average shear modulus at ambient conditions were constrained to be 154.5(6) and 89.7(4) GPa, respectively. The corresponding pressure derivatives are 4.71(10) and 1.25(5). All the above quantities were obtained from fitting the aggregate elasticity data to third-order Eulerian finite-strain equations. Previous studies of the high-pressure elastic properties of andradite-rich compositions are highly discrepant. Differences between the static compression curve derived from our data and high-pressure x-ray diffraction data can be attributed to the limited P–V coverage and the presence of small degrees of deviatoric stress in the x-ray studies. Previous high-pressure Brillouin data probably suffered from unrecognized orientation errors and/or systematic errors in velocity determination. The ambient-pressure bulk modulus obtained here is in agreement with an earlier Brillouin study, but differs significantly from the value reported by a recent ultrasonic elasticity study.

Acknowledgments

This work was supported by the National Science Foundation (EAR-0125675) and the Packard Foundation. We are grateful to Dr J Delaney, Rutgers University, for the microprobe analysis and to an anonymous reviewer whose comments improved the manuscript.

References

[1] Isaak D G 2001 *Handbook of Elastic Properties of Solids, Liquids, and Gases* ed H Bass, M Levy and R Stern (New York: Academic) Chapter 12 p 352
[2] Mao H W, Shu J F, Shen G Y, Hemley R J, Li B S and Singh A K 1998 *Nature* **396** 741–3
[3] Jacobsen S D, Spetzler H A and Reichmann H J 2002 *J. Phys.: Condens. Matter* **14** 11525–30
[4] Abramson E H, Brown J M and Slutsky L J 1999 *Annu. Rev. Phys. Chem.* **50** 279–313
[5] Duffy T S and Anderson D L 1989 *J. Geophys. Res.* **94** 1895–912
[6] Burenkov Y A and Nikaronov S P 2002 *Phys. Solid State* **44** 318–23
[7] Wang Z and Ji S 2001 *Am. Mineral.* **86** 1209–18
[8] Novak G A and Gibbs G V 1971 *Am. Mineral.* **56** 791–825
[9] Merrill L and Bassett W A 1974 *Rev. Sci. Instrum.* **45** 290–4
[10] Withfield C H, Brody E M and Bassett W A 1976 *Rev. Sci. Instrum.* **47** 942–7
[11] Speziale S and Duffy T S 2002 *Phys. Chem. Minerals* **29** 465–72
[12] Sinogeikin S V and Bass J D 2000 *Phys. Earth Planet. Inter.* **120** 43–62
[13] Jackson I and Niesler H 1982 *High Pressure Research in Geophysics* ed S Akimoto and M H Manghnani (Tokyo: Center for Academic Publications) pp 93–113
[14] Yoneda A 1990 *J. Phys. Earth* **38** 19–55
[15] Cummins H Z and Schoen P E 1972 *Laser Handbook* ed F T Arecchi and E O Schulz-Dubois (Amsterdam: North-Holland) pp 1029–76
[16] Every A G 1980 *Phys. Rev.* B **22** 1746–60
[17] Shimizu H 1995 *High Pressure Res. Solids* 1–7
[18] Zha C S, Duffy T S, Downs R T, Mao H K and Hemley R J 1996 *J. Geophys. Res.* **101** 17535–45
[19] Bass J D 1986 *J. Geophys. Res.* **91** 7505–16
[20] Jackson J M, Sinogeikin S V and Bass J D 1999 *Am. Mineral.* **84** 677–80
[21] Weidner D J and Carleton H R 1977 *J. Geophys. Res.* **82** 1334–46
[22] Birch F 1978 *J. Geophys. Res.* **83** 1257–68
[23] Birch F 1947 *Phys. Rev.* **71** 809–24
[24] Karki B B, Stixrude L and Wentzcovitch R M 2001 *Rev. Geophys.* **39** 507–34
[25] Skinner B J 1966 Thermal expansion *Handbook of Physical Constants* (*Geol. Soc. Am. Mem.*) ed S P Clark Jr pp 75–95
[26] Robie R A, Bin Z, Hemingway B S and Barton M D 1987 *Geochim. Cosmochim. Acta* **51** 2219–36
[27] Isaak D G, Anderson O L and Oda H 1992 *Phys. Chem. Minerals* **19** 106–20
[28] Chai M, Brown J M and Slutsky L J 1997 *Geophys. Res. Lett.* **24** 523–6
[29] Bass J D 1989 *J. Geophys. Res.* **94** 7621–8

[30] Babuška V, Fiala J, Kumazawa M, Ohno I and Sumino Y 1978 *Phys. Earth Planet. Inter.* **16** 157–76
[31] Milman V, Akhmatskaya E V, Nobes R H, Winkler B, Pickard C J and White J A 2001 *Acta Crystallogr.* 2B **57** 163–77
[32] Conrad P G, Zha C-S, Mao H-K and Hemley R J 1999 *Am. Mineral.* **84** 374–83
[33] Pavese A, Levy D and Pischedda V 2001 *Eur. J. Mineral.* **13** 929–37
[34] Zhang L, Ahsbahs H, Kutoglu A and Geiger C A 1999 *Phys. Chem. Minerals* **27** 52–8
[35] Hazen R H and Finger L W 1989 *Am. Mineral.* **74** 352–9